A meshless method to compute the POD and its variants from scattered data

Iacopo Tirelli[1], Miguel Alfonso Mendez[2,*], Andrea Ianiro[1] and Stefano Discetti[1]

1: Department of Aerospace Engineering, Universidad Carlos III de Madrid, Avda. Universidad 30, Leganés, 28911, Madrid, Spain
2: Environmental and Applied Fluid Dynamics, von Karman Institute for Fluid Dynamics, Waterloosesteenweg 72, Sint-Genesius-Rode,1640,Bruxelles,Belgium

*Corresponding author: mendez@vki.ac.be

Keywords: POD, RBF, meshless algorithm, PTV, PIV.

ABSTRACT

The Proper Orthogonal Decomposition (POD) is one of the most popular methods for discovering patterns from data in fluid mechanics. When the data is available on a uniform grid, such as in cross-correlation-based particle image velocimetry, the POD is equivalent to a Singular Value Decomposition (SVD) of the matrix containing the measurement. When the data is scattered, as in particle tracking velocimetry, the POD computation first requires interpolation onto a grid. Such interpolation degrades spatial resolution and limits the benefits of PTV over correlation-based methods. In this work, we propose a method to compute the POD from scattered data that circumvents the need for interpolation. The method uses physics-constrained Radial Basis Function (RBFs) regression to compute inner products in space and time. We demonstrate that this method is more accurate than the traditional interpolation or binning-based approaches. Since the method does not require the definition of a mesh and produces results that are analytic and mesh-independent, we refer to our method as meshless POD.

1. Introduction

Studying turbulent flows is challenging because of their chaotic behaviour and the large range of length and time scales involved. The "dynamical system perspective" introduced in the 90s (Holmes et al., 2012) describes turbulent flows as dynamical systems evolving on manifolds of finite dimensions, identified by a few leading "coherent structures". This promoted the interest in identifying (and objectively defining, see Jiménez (2018)) coherent structures whose dynamics could be predicted via low dimensional models. The fluid dynamics community has traditionally pursued this search via linear methods for dimensionality reduction (Mendez, 2023), although nonlinear methods from pattern identification in machine learning are gaining popularity (Farzamnik et al., 2023; Mendez, 2023).

Linear methods break the dataset as a linear combination of elementary contributions referred to as *modes*. The most ubiquitous approach for this decomposition is the Proper Orthogonal Decomposition (POD) introduced by Lumley (1967) and widely popularized by the seminal works

of Sirovich (1987, 1989, 1991). Within the image velocimetry community, this decomposition has been widely used also as a statistical filter, for example for outlier removal (Raiola et al., 2015) or image pre-processing (Mendez et al., 2017), for gap filling (Saini et al., 2016) and for resolution enhancement (Cortina-Fernández et al., 2021; Tirelli et al., 2023a). Moreover, many variants and hybrid formulations of the POD have been introduced, such as Gappy POD (Everson et al., 1997), Spectral POD (Sieber et al., 2016) or Multiscale POD (Mendez et al., 2019) to mention a few.

These decompositions can be easily implemented as matrix factorizations when the data is available on a regular and fixed grid, as in traditional cross-correlation-based image velocimetry. In the case of the POD, it is easy to show that this corresponds to a Singular Value Decomposition (Dawson, 2023). However, the implementation is considerably more cumbersome when the data is scattered.

Scattered data is produced by Particle Tracking Velocimetry (PTV), which has been gaining prominence in recent years, especially for 3D velocimetry, thanks to advanced tracking algorithms (Schanz et al., 2016; Tan et al., 2020). Tracking velocimetry allows for measuring local velocity without the modulation effects produced by cross-correlation, thus offering much higher resolutions. A common approach to leverage 3D PTV while maintaining most of the post-processing algorithms developed for structured data is to resort to data interpolation methods, potentially enhanced by physics-based constraints (Schneiders & Scarano, 2016; Gesemann et al., 2016). Nevertheless, all interpolation methods lose at least some of the resolution gains achieved by PTV.

This work departs from traditional post-processing approaches by introducing a novel, meshless (analytical) formulation of POD for PTV that requires neither interpolation nor binning. The proposed method uses the constrained Radial Basis function regression introduced in (Sperotto et al., 2022) to compute inner products in space and time. We show that this provides higher accuracy than the usual interpolation-based approach and provides an analytical (mesh-independent) representation of the spatial structures. The theoretical background of the methodology is detailed in Section 2, while the validation is presented in Section 3 on two different synthetic datasets: the wake of a fluidic pinball and the turbulent channel flow.

2. Methodology

The proposed methodology follows the classic snapshot-based POD by Sirovich (1991). The cornerstone of our method is that all inner products are formulated in an RBF formulation that requires no grid and thus no interpolation. The data can be scattered both in space and time. The final result is a linear decomposition of the data in the form:

$$u(\mathbf{x}, t_i) = \sum_{r=1}^{r_c} \sigma_r \phi_r(\mathbf{x}) \psi_r(t) \,, \tag{1}$$

where σ_r are scalars defining the amplitude of each contribution, $\phi_r(\mathbf{x})$ and $\psi_r(t)$ are the spatial and the temporal structures of the POD modes.

The meshless POD procedure is outlined in the steps below.

Step 1: Analytical snapshot representation with RBF

Starting from scattered data available for the different time realizations, an analytical approximation of the field for each time instant is obtained as a linear combination of a set of basis functions. This approximation is denoted as:

$$\tilde{u}(\mathbf{x}, t_i) = \sum_{q=1}^{N_b} w_q(t_i)\gamma_q(\mathbf{x}), \tag{2}$$

where N_b is the number of basis functions used in the approximation, γ_q is the q^{th} regression basis, and w are the corresponding weights. The vector $\mathbf{x}$ contains the coordinates on which the data are evaluated at the i^{th} time instant t_i among the total N_t time instances. With no loss of generality, the basis functions employed in this work are thin-plate radial basis functions (RBF). These only require the definition of the collocation and have no shape factor parameters. We use the vector coordinates $\mathbf{x}_p$ as collocation. Therefore, the current approach has no hyper-parameters to tune, needs no user input and only requires extra memory storage for the weights. Future work will explore more advanced formulations and the use of physics constraints as in Sperotto et al. (2022).

Step 2: Temporal correlation matrix

The temporal correlation matrix $\mathbf{K} \in \mathbb{R}^{N_t \times N_t}$ is defined as the matrix whose elements are the inner products in space, denoted as $\langle \cdot, \cdot \rangle_s$, between all the snapshots:

$$\mathbf{K} = \begin{bmatrix} \langle u_1, u_1 \rangle_s & \langle u_1, u_2 \rangle_s & \dots & \langle u_1, u_{Nt} \rangle_s \\ \langle u_2, u_1 \rangle_s & \langle u_2, u_2 \rangle_s & \dots & \langle u_2, u_{Nt} \rangle_s \\ \vdots & \vdots & \ddots & \vdots \\ \langle u_{Nt}, u_1 \rangle_s & \langle u_{Nt}, u_2 \rangle_s & \dots & \langle u_{Nt}, u_{Nt} \rangle_s \end{bmatrix} \tag{3}$$

In the original formulation (Lumley, 1967) of the POD, the inner product in space or time were defined in terms of correlation of square-integrable real-valued functions, that is:

$$K_{ij} = \frac{1}{\parallel \Omega \parallel} \int_{\Omega} \tilde{u}(\mathbf{x}, t_i)\ \tilde{u}(\mathbf{x}, t_j)\ d\Omega\,, \tag{4}$$

with Ω the spatial domain considered. If Ω is partitioned in uniform N_s elements of area (or volume) $\Delta\Omega$, indexed by $k \in [0, N_s - 1]$ a straightforward approximation approximation of Eq. (4) reads as

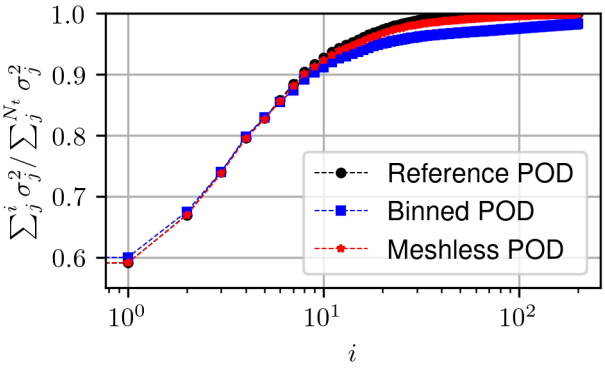

Figure 1. Comparison of the energy distribution for the fluidic pinball. The reference POD is represented by the black curves with circle markers, while the red curve with star markers depicts the meshless approach, and the blue curve with square markers represents the binned method. On the x-axis is denoted the index of the mode.

$$K_{ij} \approx \frac{1}{N_s \Delta\Omega} \sum_k \tilde{u}(\mathbf{x}_k, t_i)\, \tilde{u}(\mathbf{x}_k, t_j)\, \Delta\Omega = \frac{1}{N_s} \mathbf{u}_j^T \mathbf{u}_i \,, \tag{5}$$

where $\mathbf{u}_i, \mathbf{u}_j \in \mathbb{R}^{N_s}$ are the vectors collecting the data sampled at time steps i and j and corresponding to each of the N_s portions of the spatial domain. In this setting, the correlation matrix can be computed using a simple matrix multiplication as $\mathbf{K} = \mathbf{U}^T\mathbf{U}$. Eq. (5) is an approximation of (4) using the mid-point rule (Griffiths & Smith, 2006), that is assuming a piecewise-constant approximation of the velocity field.

POD algorithms for gridded data use Eq. (5). Interpolation-based formulations for PTV seek to bring the scattered data onto a uniform grid so that Eq. (5) can still be used. We here propose to use the original version in Eq. (4), leveraging the regression of Eq. (2) in step 1 and a quadrature method that interrogates the integrand on specific quadrature points. With no loss of generality, we here use Gauss-Legendre quadrature because of its excellent trade-off between accuracy and computational costs. It is worth stressing that quadrature methods using analytic approximations of the integrand are much more accurate than the mid-point rule implied in Eq. (5).

Step 3: Computing Temporal Structures

The eigenvectors of the temporal correlation matrix are the temporal structure of the POD modes. Therefore, given the temporal correlation matrix, these reads

$$\mathbf{K} = \Psi \Sigma^2 \Psi^T, \tag{6}$$

where the matrix $\Psi \in \mathbb{R}^{n_t \times r_c}$ collects the eigenvectors along its columns and Σ is a diagonal matrix whose elements σ_i represent the mode amplitudes (cf. Eq. 2). This step is identical to the classic snapshot POD for grid data.

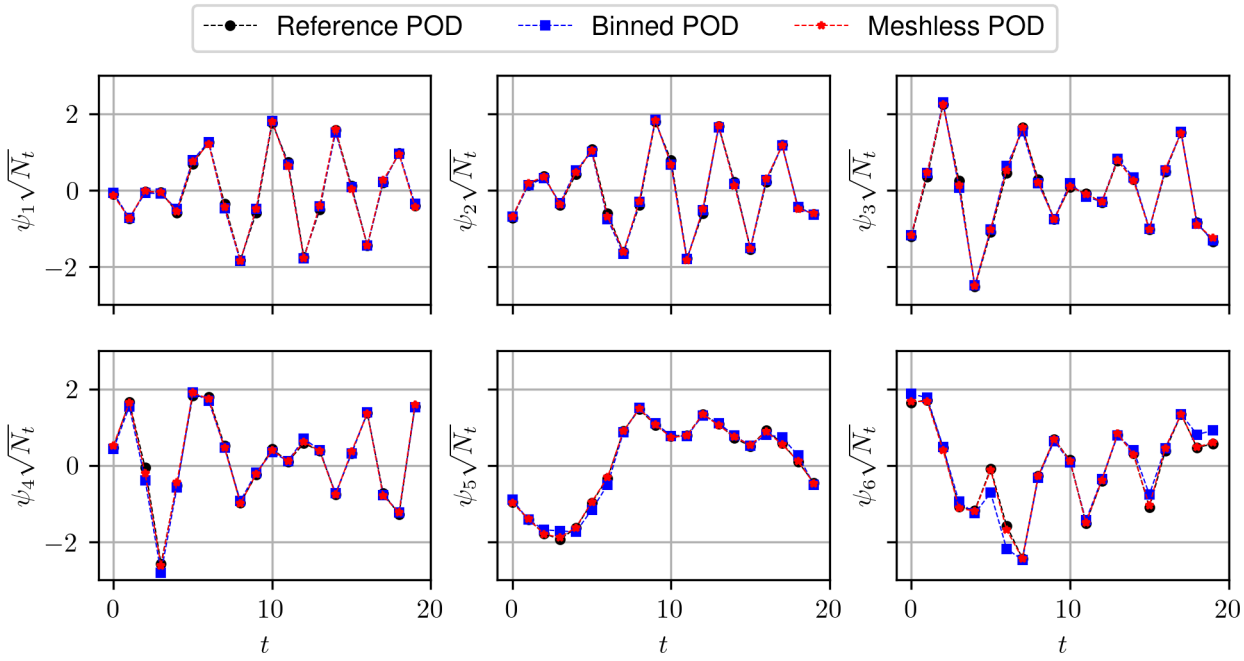

Figure 2. Comparison of the distribution of the r^{th} temporal mode ψ_r for the fluidic pinball. The reference POD is represented by the black curves with circle markers, while the red curve with star markers depicts the meshless approach, and the blue curve with square markers represents the binned one. On the x-axis is denoted the corresponding time instant. Only the first 20 time instants are displayed.

Step 4: Computing Spatial Structures

The r^{th} spatial structure ϕ_r is the result of projecting the dataset $\tilde{u}(x,t)$ onto the temporal structure ψ_r. This project requires an inner product in time. The same discussion in Step 2 now applies to the inner product in the time domain, which reads

$$\phi_r(\mathbf{x}) = \frac{1}{\sigma_r}\langle \tilde{u}(\mathbf{x},t), \psi_i(\mathbf{t})\rangle = \frac{1}{\sigma_r T}\int_t \tilde{u}(\mathbf{x},\mathbf{t})\ \psi_r(\mathbf{t})\ dt\ \approx \frac{1}{\sigma_r N_t}\sum_{k=1}^{N_t}\tilde{u}(\mathbf{x},\mathbf{t}_k)\psi_r(\mathbf{t}_k) \tag{7}$$

assuming that the time domain is $t \in [0,T]$. Here both the temporal structures and the regression of the snapshots are available on a discrete set of times $\mathbf{t} \in \mathbb{R}^{N_t}$. Although advanced quadratures could also be used in Eq. (7) together with an analytic regression in time, the gain in accuracy was considered not worth the additional computational cost. Therefore, in this work, this projection is carried out via mid-point approximation in time.

We stress that Eq. (7) holds for *any* set of points $\mathbf{x}$. Hence Eq. (7) enables in principle super-resolution of the POD modes. In this work, we compute it over a uniform grid for plotting purposes and compare it with interpolation-based approaches.

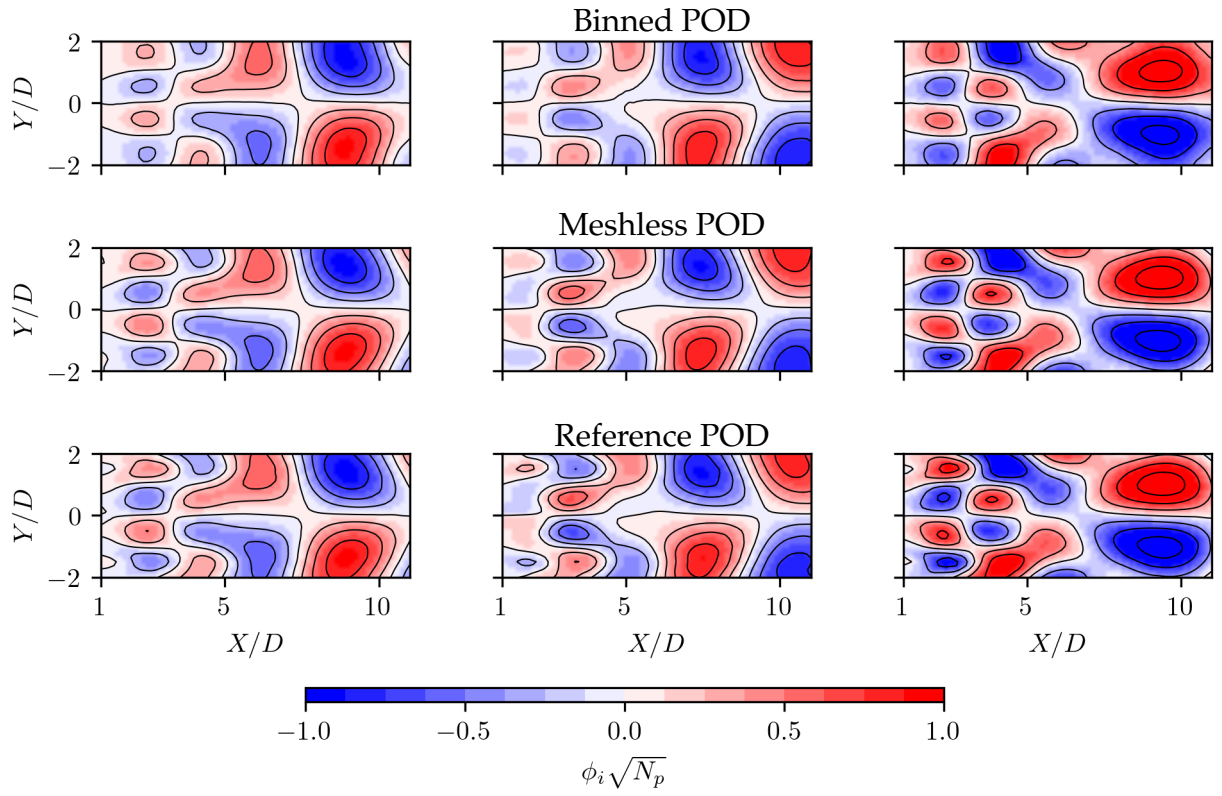

Figure 3. Comparison of the spatial modes ϕ_i associated to the steamwise velocity component u for the fluidic pinball. The reference POD is represented in the third row, while the binned and the meshless approaches are displayed in the first and the second row, respectively. Only the first three modes are pictured.

3. Validation

3.1. Fluidic pinball

The first test case is the wake of a fluidic pinball, a configuration of three cylinders with diameter D located at the vertices of an equilateral triangle. Direct Numerical Simulation (DNS) data from Deng et al. (2020) is used for this case. The DNS data consists of an unstructured grid with 3536 points within the domain $x/D \in [1, 11]$ and $y/D \in [-2, 2]$ (with x, y being the stream-wise and cross-wise directions, respectively). We arbitrarily define a scaling factor of 32 pixels per diameter, which produces a particle density of $N_{ppp} = 0.086$ (particles per pixel). To define the ground truth for the POD computation, we interpolate the data on a fine grid with $\Delta x = D/16$ and compute the POD with the traditional matrix factorization approach. We consider the resulting modes as **“reference POD"**.

We then consider a subset with particle concentration of $N_{ppp} = 0.0086$ (i.e. 10 times lower) to simulate PTV measurements. This is used to test the meshless POD computation, and the results are referred to as “meshless POD". The mapping onto a regular grid is carried out using a moving

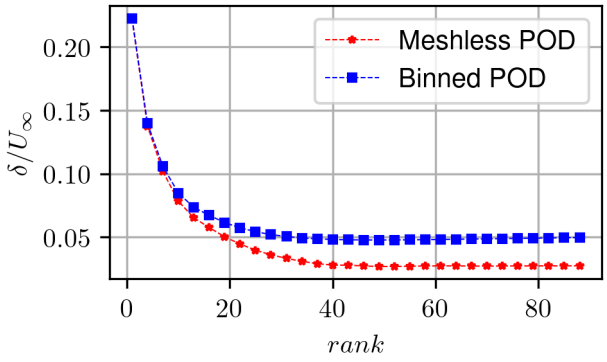

Figure 4. Comparison of the root mean square error δ_{RMS}, normalized with respect to the freestream velocity U_∞, of the reconstruction at different ranks for the case of the fluidic pinball. The red curve with star markers depicts the meshless approach, while the blue curve with square markers represents the binned method.

	$\delta_{\text{RMS}}/\text{rms}(\psi_{\text{ref}_i})$					
	ψ_1	ψ_2	ψ_3	ψ_4	ψ_5	ψ_6
Binned POD	0.0604	0.0612	0.0896	0.1307	0.0938	0.1921
Meshless POD	0.0600	0.0605	0.0576	0.0589	0.0271	0.0462

Table 1. Root mean square error δ_{RMS} evaluated for both binned and meshless approaches for the i^{th} temporal mode, divided by the standard deviation of its corresponding DNS mode ψ_{ref_i}.

average with windows of 32 pixels. This simulates a cross-correlation-based interrogation or the binning of the PTV data onto a regular grid, from which the classic matrix-factorization approach for the POD is employed. In what follows, we refer to the results of this approach on the binned data as “binned POD".

Since the dataset is statistically stationary, focus is placed on the decomposition of the fluctuating component of the velocity field. To ensure a fair comparison across the methodologies, the Ensemble PTV high-resolution mean is subtracted from the entire fields from all the datasets as explained in Tirelli et al. (2023b). The results of the decomposition are shown in Figs. 1, 2 and 3. Fig. 1 shows the distribution of normalized amplitudes for all the methodologies across the modes. This plot reveals a first discrepancy among the two methodologies when compared to the DNS: the curve of the meshless approach is closer to the reference while the PIV seems to lose some of the energy related to the higher modes. This discrepancy arises from the moving average process produced by the cross-correlation, which tends to filter out the smallest scales.

Fig. 2 shows the first six temporal structures ψ_i normalized with the square root of the number of samples N_t. Notably, discrepancies become larger as higher-order modes are considered. This kind of comparison is limited to the leading modes: since less energetic modes tend to differ in the two approaches due to the different resolutions, the ordering between modes can significantly differ and produce largely different decompositions. However, the illustrated modes suggest that the

	$\delta_{\text{RMS}}/\text{rms}(\phi_{\text{ref}_i})$		
	ϕ_1	ϕ_2	ϕ_3
Binned POD	0.1466	0.1483	0.1993
Meshless POD	0.0665	0.0708	0.0669

Table 2. Root mean square error δ_{RMS} evaluated for both binned and meshless approaches for the i^{th} spatial mode, divided by the rms of its corresponding DNS mode ϕ_{ref_i}.

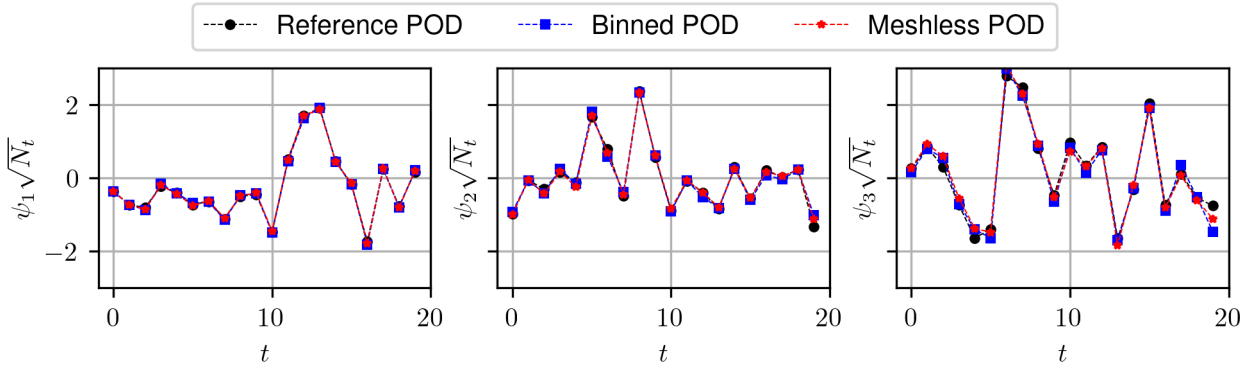

Figure 5. Comparison of the distribution of the i^{th} temporal mode ψ_i for the turbulent channel flow. The reference POD is represented by the black curves with circle markers, while the red curve with star markers depicts the meshless approach, and the blue curve with square markers represents the binned method. On the x-axis is denoted the corresponding time instant, for a better visualization only the first 20 are displayed.

meshless approach closely follows the reference from the DNS. The relative RMSE in the temporal structures, computed with respect to the reference modes from DNS, is shown in Tab. 1.

The first 3 spatial modes ϕ_i associated with the stream-wise velocity component U are analysed in Fig. 3. Looking at the contours in Fig. 3, the PIV modes seem more attenuated if compared to the ones computed with the meshless approach. Table 2 collects the relative RMSE δ_{RMS} for the first three modes with respect to the reference modes from DNS, proving that the proposed meshless approach better evaluated for the same three spatial modes normalized with the RMS of the corresponding DNS modes.

3.2. Turbulent Channel Flow

The second test case is the DNS of a turbulent channel flow, which is accessible through the Johns Hopkins Turbulence Database (`http://turbulence.pha.jhu.edu/`). This test case poses greater challenges due to the more chaotic nature of the flow behaviour and the larger range of turbulent length scales involved. The reader is referred to Li et al. (2008) for details on the simulations. The data is interpolated on a uniform grid with a spacing of 4 pixels that spans a domain of $x/h \in [0, 0.5]$ and $y/h \in [0, 0.5]$, where h represents the half-channel- heights. The particle den-

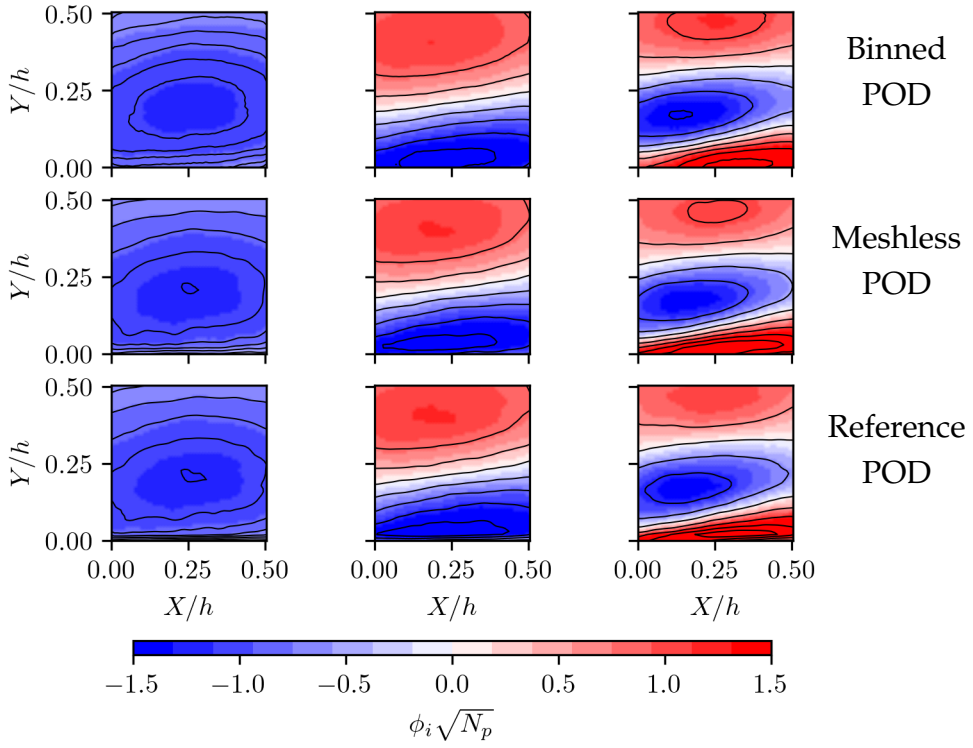

Figure 6. Comparison of the spatial modes ϕ_i associated to the steamwise velocity component u for the turbulent channel flow. The reference POD is represented in the third row, while the binned and the meshless approaches are displayed in the first and the second row, respectively. Only the first three modes are pictured.

sity N_{ppp} is 0.01 (4096 particles). The same steps of the previous test case are employed to establish the ground truth and the synthetic PTV and PIV with an interrogation window of 32 pixels.

The validation performed for this test case follows the same procedure as described in Sec.3.1. Temporal and spatial modes are illustrated in Fig. 5 and Fig. 6, respectively. Building upon the insights from the previous section, we can now focus our comparison solely on the first three modes since the increased complexity of this test case tends to introduce order mixing among the subsequent modes. However, for both temporal and spatial cases, the figures confirm what is already seen in the previous test case. The RMSE values reported in Tabs. 3-4 confirm quantitatively this difference.

The velocity field reconstructions are presented in Fig. 7. Notably, the meshless POD exhibits higher accuracy compared to the traditional PIV approach, as evidenced by the lower error. The RMSE curve, normalised with the bulk velocity U_b shows a minimum for the meshless POD, with a value of 0.0243, compared to 0.0294 for the traditional PIV. This improvement in accuracy further demonstrates the effectiveness of the meshless POD methodology in capturing and reconstructing complex flow patterns with higher precision.

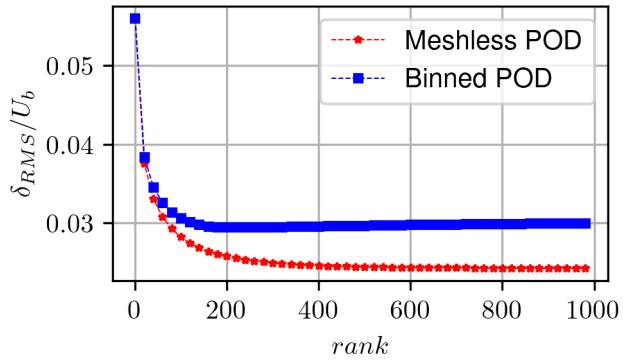

Figure 7. Comparison of the RMSE on the reconstruction with different ranks for the turbulent channel flow. The red curve with star markers depicts the meshless approach, and the blue curve with square markers represents the binned method.

	$\delta_{\text{RMS}}/\text{rms}(\psi_{\text{ref}_i})$		
	ψ_1	ψ_2	ψ_3
Binned POD	0.0354	0.0904	0.1835
Meshless POD	0.0250	0.0762	0.1726

Table 3. Root mean square error δ_{RMS} evaluated for both binned and meshless approaches for the i^{th} temporal mode, divided by the standard deviation of its corresponding DNS mode ψ_{ref_i}.

4. Conclusions

We propose a novel approach to compute the POD of scattered data produced via PTV, avoiding the need for interpolation onto a structured fixed grid. The approach uses the RBF regression and advanced quadrature to compute inner products in space and time and provides an analytic (mesh-independent) representation of the POD modes. The approach avoids the modulation effects associated with mapping PTV measurements onto a Cartesian grid. Moreover, the quadrature methods enabled by the RBF regression allow for more accurate computation of the temporal correlation matrix and, hence, the temporal structures of the POD modes. We show that the method allows recovering scales filtered out by binning onto a regular grid. The method can be readily applied to variants of the POD, such as SPOD or mPOD. Besides these extensions, ongoing work

	$\delta_{\text{RMS}}/\text{rms}(\phi_{\text{ref}_i})$		
	ϕ_1	ϕ_2	ϕ_3
Binned POD	0.0750	0.1458	0.1936
Meshless POD	0.0293	0.0768	0.1086

Table 4. Root mean square error δ_{RMS} evaluated for both binned and meshless approaches for the i^{th} spatial mode, divided by the standard deviation of its corresponding DNS mode ϕ_{ref_i}.

includes the test on experimental test cases (2D and 3D), while future work will seek to include more advanced and memory-efficient RBF regression methods.

Acknowledgment

This project has received funding from the European Research Council (ERC) under the European Union's Horizon 2020 research and innovation program (grant agreement No 949085). However, the views and opinions expressed are those of the authors only and do not necessarily reflect those of the European Union or the European Research Council. Neither the European Union nor the granting authority can be held responsible for them.

References

Cortina-Fernández, J., Sanmiguel Vila, C., Ianiro, A., & Discetti, S. (2021). From sparse data to high-resolution fields: ensemble particle modes as a basis for high-resolution flow characterization. *Experimental Thermal and Fluid Science*, *120*, 110178.

Dawson, S. (2023). The proper orthogonal decomposition. In M. A. Mendez, A. Ianiro, B. R. Noack, & S. L. Brunton (Eds.), *Data-driven fluid mechanics: Combining first principles and machine learning* (p. 117–132). Cambridge University Press.

Deng, N., Noack, B. R., Morzyński, M., & Pastur, L. R. (2020). Low-order model for successive bifurcations of the fluidic pinball. *Journal of fluid mechanics*, *884*, A37.

Everson, R., Cornillon, P., Sirovich, L., & Webber, A. (1997). An empirical eigenfunction analysis of sea surface temperatures in the western north atlantic. *Journal of Physical Oceanography*, *27*(3), 468–479.

Farzamnik, E., Ianiro, A., Discetti, S., Deng, N., Oberleithner, K., Noack, B., & Guerrero, V. (2023). From snapshots to manifolds – a tale of shear flows. *Journal of Fluid Mechanics*, *955*.

Gesemann, S., Huhn, F., Schanz, D., & Schröder, A. (2016). From noisy particle tracks to velocity, acceleration and pressure fields using b-splines and penalties. In *18th international symposium on applications of laser techniques to fluid mechanics.*

Griffiths, D. V., & Smith, I. (2006). *Numerical methods for engineers*. Routledge, Taylor & Francis.

Holmes, P., John L. Lumley, G. B., & Rowley, C. W. (2012). *Turbulence, coherent structures, dynamical systems and symmetry*. Cambridge Monographs on Mechanics.

Jiménez, J. (2018). Coherent structures in wall-bounded turbulence. *Journal of Fluid Mechanics*, *842*, P1.

Li, Y., Perlman, E., Wan, M., Yang, Y., Meneveau, C., Burns, R., … Eyink, G. (2008). A public turbulence database cluster and applications to study Lagrangian evolution of velocity increments in turbulence. *Journal of Turbulence*(9), N31.

Lumley, J. L. (1967). The structure of inhomogeneous turbulent flows. *Atmospheric turbulence and radio wave propagation*, 166–178.

Mendez, M. (2023). Generalized and multiscale modal analysis. In M. A. Mendez, A. Ianiro, B. R. Noack, & S. L. Brunton (Eds.), *Data-driven fluid mechanics: Combining first principles and machine learning* (p. 153–181). Cambridge University Press.

Mendez, M., Balabane, M., & Buchlin, J.-M. (2019). Multi-scale proper orthogonal decomposition of complex fluid flows. *Journal of Fluid Mechanics*, *870*, 988–1036.

Mendez, M., Raiola, M., Masullo, A., Discetti, S., Ianiro, A., Theunissen, R., & Buchlin, J.-M. (2017). POD-based background removal for particle image velocimetry. *Experimental Thermal and Fluid Science*, *80*, 181–192.

Raiola, M., Discetti, S., & Ianiro, A. (2015). On PIV random error minimization with optimal POD-based low-order reconstruction. *Experiments in fluids*, *56*, 1–15.

Saini, P., Arndt, C. M., & Steinberg, A. M. (2016). Development and evaluation of gappy-POD as a data reconstruction technique for noisy PIV measurements in gas turbine combustors. *Experiments in Fluids*, *57*, 1–15.

Schanz, D., Gesemann, S., & Schröder, A. (2016, 04). Shake-The-Box: Lagrangian particle tracking at high particle image densities. *Experiments in Fluids*, *57*.

Schneiders, J., & Scarano, F. (2016, 08). Dense velocity reconstruction from tomographic PTV with material derivatives. *Experiments in Fluids*, *57*.

Sieber, M., Paschereit, C. O., & Oberleithner, K. (2016). Spectral proper orthogonal decomposition. *Journal of Fluid Mechanics*, *792*, 798–828.

Sirovich, L. (1987). Turbulence and the dynamics of coherent structures. i. coherent structures. *Quarterly of applied mathematics*, *45*(3), 561–571.

Sirovich, L. (1989). Chaotic dynamics of coherent structures. *Physica D: Nonlinear Phenomena*, *37*(1-3), 126–145.

Sirovich, L. (1991). Analysis of turbulent flows by means of the empirical eigenfunctions. *Fluid Dynamics Research*, *8*(1-4), 85.

Sperotto, P., Pieraccini, S., & Mendez, M. A. (2022). A meshless method to compute pressure fields from image velocimetry. *Measurement Science and Technology*, *33*(9), 094005.

Tan, S., Salibindla, A., Masuk, A. U. M., & Ni, R. (2020). Introducing OpenLPT: new method of removing ghost particles and high-concentration particle shadow tracking. *Experiments in Fluids*, *61*(47).

Tirelli, I., Ianiro, A., & Discetti, S. (2023a). An end-to-end KNN-based PTV approach for high-resolution measurements and uncertainty quantification. *Experimental Thermal and Fluid Science*, *140*, 110756.

Tirelli, I., Ianiro, A., & Discetti, S. (2023b). A simple trick to improve the accuracy of PIV/PTV data. *Experimental Thermal and Fluid Science*, *145*, 110872.